photonics

MDPI

Article

Plasma Physics-Based Deep Learning Modeling for Accurate Morphology Prediction in Femtosecond Bessel Laser Processing of ZnS

Yifan Deng [1,2], Jingya Sun [1,2,*], Manlou Ye [1], Xiaokang Dong [1,2], Xiang Li [1,2] and Yang Yang [3]

[1] Laser Micro/Nano Fabrication Laboratory, School of Mechanical Engineering, Beijing Institute of Technology, Beijing 100081, China; 3220230341@bit.edu.cn (Y.D.); 3120215234@bit.edu.cn (M.Y.); 3220250356@bit.edu.cn (X.D.); 3220230340@bit.edu.cn (X.L.)
[2] Yangtze Delta Region Academy of Beijing Institute of Technology, Jiaxing 314000, China
[3] Beijing National Laboratory for Condensed Matter Physics, Institute of Physics, Chinese Academy of Sciences, P.O. Box 603, Beijing 100190, China; yang.yang@iphy.ac.cn
* Correspondence: sjy@bit.edu.cn

Abstract

Femtosecond laser processing has become a powerful approach for high-precision micro- and nanofabrication in transparent materials, owing to its ultrashort pulse duration and minimized thermal effects. However, the limited predictability of processing depth remains a major obstacle to practical applications. Here, we present a morphology prediction framework for femtosecond Bessel laser processing of ZnS that integrates plasma physics modeling with deep learning. Through combined experimental measurements and plasma physics simulations, the influence of laser pulse energy on electron density evolution and material removal depth is systematically investigated. The results reveal the dominant roles of multiphoton ionization, avalanche ionization, and free-electron dynamics in deep-volume processing, and demonstrate the strong sensitivity of the processing morphology to the plasma distribution. Conventional plasma models can accurately reproduce the ablation diameter, yet exhibit significant limitations in predicting the processing depth. We propose a physics data-based framework for femtosecond Bessel beam processing, which integrates a depth-residual regression network conditioned on the peak electron density distribution to effectively learn and compensate for systematic modeling errors in plasma-based simulations. This strategy leads to excellent agreement between predicted and experimental processing depths and three-dimensional morphologies under various energy conditions. The model achieves a mean absolute error (MAE) of 4.9 nm at the pixel level for 3D crater reconstruction. Under rigorous crater-grouped cross-validation with Leave-One-Group-Out evaluation, the model achieves a mean R^2 of 0.74 across 8 independent craters, demonstrating reliable generalization to unseen energy conditions. These results demonstrate that incorporating physical priors into data-driven learning provides an effective pathway to overcoming accuracy limitations in modeling complex laser–matter interactions. This approach offers a reliable tool for quantitative prediction and parameter optimization in deep femtosecond laser processing of transparent materials and enabling highly controllable and reproducible micro- and nanofabrication for advanced photonic and three-dimensional optical applications.

Keywords: femtosecond laser processing; zinc sulfide (ZnS); plasma dynamics; deep learning

Check for updates

Received: 26 March 2026
Revised: 14 April 2026
Accepted: 15 April 2026
Published: 20 April 2026

Copyright: © 2026 by the authors. Licensee MDPI, Basel, Switzerland. This article is an open access article distributed under the terms and conditions of the Creative Commons Attribution (CC BY) license.

1. Introduction

Femtosecond laser processing, with its ultrashort pulses and non-thermal interactions, has become a powerful approach for precise micro- and nanofabrication in transparent materials [1–5]. The ultrafast nature of femtosecond pulses allows energy deposition faster than thermal diffusion timescales, minimizing collateral heating and enabling true non-thermal material processing. These capabilities have been successfully applied across a wide range of materials, including sapphire, silicon carbide ceramics, and polymer microstructures. For instance, three-dimensional surface micro-structuring of sapphire has been achieved with sub-micrometer precision [6], silicon carbide ceramics have been polished to optical-grade smoothness [2], and selective deposition of graphene oxide on polymer microstructures has been realized for functional device fabrication [7]. In transparent materials such as zinc sulfide (ZnS), femtosecond laser processing enables the creation of high-quality internal modifications and precise surface patterns, which are critical for advanced photonic and optoelectronic devices [8,9]. ZnS is widely used in thermal imaging windows and multispectral optical systems due to its broad transparency range (0.4–14 μm). Recent studies have further demonstrated diverse femtosecond laser micro-machining capabilities on ZnS, including Bessel-beam-based antireflective structures [10], biomimetic high-aspect-ratio micro hole arrays [11], and micro-optical elements on ZnS ceramics [12]. However, the wide bandgap and relatively low thermal conductivity of ZnS present unique challenges for ultrafast laser processing, necessitating accurate predictive models for process optimization.

Despite the transformative potential of femtosecond lasers, conventional Gaussian beams are inherently limited by their short Rayleigh lengths, which constrain the focal depth and the achievable volumetric modification in thick transparent materials [13–15]. As a result, multiple refocusing steps and precise sample positioning are often required, increasing process complexity and reducing throughput. In contrast, Bessel beams possess a non-diffracting propagation characteristic and an extended depth of focus, maintaining a narrow central core with nearly invariant transverse energy distribution over long propagation distances [15–19]. This unique property allows Bessel beams to generate continuous, high-aspect-ratio microstructures within transparent materials, such as optical waveguides, microchannels, or internal voids, while reducing sensitivity to sample alignment and surface irregularities. Recent advances have further demonstrated the capability of ultrafast Bessel beams to achieve extreme aspect ratios in various transparent materials [20], highlighting the growing importance of predictive modeling tools for deep material modification. Nevertheless, accurate prediction of processing depth remains a significant challenge. The interaction of femtosecond Bessel beams with materials is governed by complex multiphoton and avalanche ionization dynamics, resulting in free-electron plasma generation, localized refractive index changes, nonlinear absorption, and beam defocusing [21–23]. Recent studies have further investigated the distinctive characteristics of Bessel–Gaussian beams in laser–plasma interactions, revealing that their non-diffracting propagation can significantly modulate the spatial distribution of plasma and energy deposition profiles [24,25]. In addition, the energy coupling behavior under different material environments has been systematically analyzed, highlighting the sensitivity of plasma evolution to both beam structure and medium properties [26]. These studies provide important physical insights for constructing plasma-based simulation models. However, traditional plasma-based models attempt to simulate these phenomena to predict modification depth; however, their accuracy is highly sensitive to material parameters such as multiphoton ionization cross-sections, avalanche ionization coefficients, and plasma absorption coefficients, which are difficult to measure precisely and can vary under different laser conditions [27,28]. Moreover, simplifications inherent in these models, including uniform material assumptions or neglecting dynamic plasma plume effects, often

result in discrepancies between simulations and experiments [29,30]. Additional dynamic processes, including laser-induced shockwaves and plasma plume expansion, introduce further complexity that conventional models fail to fully capture [31–33].

To overcome these limitations, integrating deep learning with physics-based simulations offers a promising avenue for improving predictive accuracy. Deep learning excels at capturing complex, nonlinear relationships and extracting hidden patterns from large datasets [34]. By combining experimental data with physics-based simulations, machine learning models can learn systematic deviations in plasma-based predictions and account for effects that are difficult to model analytically, such as dynamic plasma behavior, scattering, and energy redistribution. Recent studies have demonstrated the feasibility of such approaches in femtosecond laser processing, for example, by predicting the three-dimensional morphology of sapphire surfaces based on laser parameters using regression models. Unlike purely data-driven approaches [18], which directly map macroscopic laser parameters (e.g., power, repetition rate, pulse number) to drilling depth without physical modeling, this work proposes a physics-informed hybrid framework with three key differences. First, instead of low-dimensional laser parameters, we use physically meaningful plasma-simulation descriptors, namely the spatiotemporal evolution of peak electron density, which encodes nonlinear ionization dynamics in laser–material interaction. Second, rather than learning a direct mapping, we adopt residual learning to predict the gap between physics-based outputs and experimental measurements, reducing complexity and focusing on compensating systematic errors such as simplified ionization models and neglected post-pulse effects. Third, by embedding physical priors into the feature space, the framework achieves reliable performance with much less training data, while conventional data-driven methods typically require large datasets. This combination of data-driven learning with physical insight provides a powerful framework for improving depth control in high-aspect-ratio transparent material processing.

The motivation for this study arises from the critical need for precise control over micro- and nano-scale structures in transparent materials, where the performance of optical and electronic devices is highly sensitive to the geometry and depth of internal modifications [35–37]. While Bessel beams provide a robust means of achieving continuous, high-aspect-ratio modifications, the lack of accurate predictive tools limits process optimization, repeatability, and the scalability of femtosecond laser fabrication. Addressing these challenges is essential for advancing applications such as integrated photonic circuits, microfluidic channels, and three-dimensional diffractive optical elements [38–42].

This work aims to develop a hybrid framework that integrates plasma-based physical modeling with deep learning to predict femtosecond Bessel beam processing depths in ZnS with high precision. In this work, we develop a plasma-based physical model of ZnS under femtosecond Bessel beam irradiation and use it to generate a comprehensive set of simulation data across a wide range of laser parameters. The discrepancies between the model predictions and experimental measurements are then analyzed, leading to a deep-learning correction strategy that compensates for the intrinsic limitations of the physical model. The proposed framework is further validated through experiments, confirming its ability to provide accurate and reliable guidance for high-aspect-ratio micro- and nano-fabrication in transparent materials. This hybrid approach improves predictive accuracy and supports the design and optimization of femtosecond laser processing protocols, enabling reproducible and precise fabrication of advanced photonic and optoelectronic devices.

2. Materials and Methods

2.1. Femtosecond Laser Processing and Ultrafast Characterization of ZnS

To investigate femtosecond laser processing and ultrafast carrier dynamics in zinc sulfide (ZnS), experiments combining Bessel-beam processing and pump–probe characterization were performed.

An axicon-based optical system was constructed to generate a Bessel beam from a 1030 nm femtosecond laser source (YactoCrystal-FL-20, Hangzhou Yacto Technology Co., Ltd., Hangzhou, China). As illustrated in Figure 1a, the incident Gaussian beam was converted into a Bessel beam using an axicon (GCL-114012, Daheng Optics, Beijing, China) with a base angle of $\beta = 2°$. In this study, the axicon apex angle was set to $\alpha_0 = 2°$, producing an output cone angle of $\beta = 0.91°$ and a maximum depth of focus of $z_{max} = 157.7$ mm. The diameter of the Bessel beam's central lobe, determined by its first-order zero, was 38.66 μm. A 4f imaging system consisting of a plano-convex lens ($f_1 = 150$ mm) and a 20× objective lens ($f_2 = 9$ mm) from Thorlabs, Newton, NJ, USA, was employed to demagnify the Bessel beam. The system magnification was $\Gamma = f_1/f_2 = 16.67$. After passing through the 4f system, the Bessel beam exhibited a transformed cone angle of $\beta' = 14.79°$ and a corresponding depth of focus of $z'_{max} = 567.8$ μm. The generation principle of the Bessel beam and its characteristic non-diffracting propagation are schematically shown in Figure 1b.

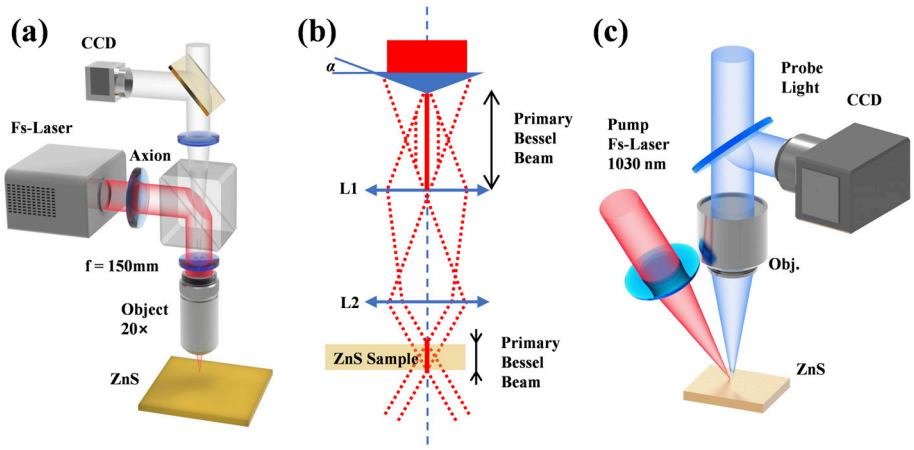

Figure 1. Bessel-beam setup and pump–probe diagnostics for ZnS processing. (**a**) Axicon-based generation of a 1030 nm Bessel beam for deep ZnS processing. (**b**) Formation principle showing non-diffracting core and concentric rings. (**c**) Reflective pump-probe setup for probing ultrafast laser-matter interaction.

Single-pulse laser irradiation experiments were conducted on ZnS samples using this optical configuration. The resulting microstructures were subsequently characterized using confocal microscopy (OLX5100, Olympus, Tokyo, Japan) to evaluate the morphology of the processed regions. To further investigate the ultrafast dynamics induced by femtosecond laser excitation, a reflective pump–probe system was employed, as shown in Figure 1c. The pump beam excited the ZnS sample while a time-delayed probe beam monitored the transient reflectivity changes. By varying the optical delay between the pump and probe pulses, time-resolved reflectivity maps of the excited region were recorded, enabling the characterization of carrier dynamics during and after laser excitation.

2.2. Plasma-Based Simulation Framework

To model the interaction between femtosecond laser pulses and ZnS, a plasma dynamics framework was established that integrates multiphoton ionization, collisional ionization, and Drude free-electron dynamics. Multiphoton ionization initiates the generation of seed electrons under high-intensity ultrashort pulses, while collisional ionization

leads to avalanche multiplication of carriers. The Drude model describes the macroscopic response of the free-electron plasma, including energy absorption and scattering processes.

The overall numerical workflow is illustrated in Figure 2. The simulation framework couples laser-field propagation, plasma generation, and subsequent energy transfer processes to describe the interaction between a femtosecond Bessel beam and dielectric materials. The computational procedure begins with the initialization of optical-system parameters and discretization of the spatial–temporal domain. Subsequently, the laser intensity distribution is calculated and used as the driving source for plasma generation. The evolution of free-electron density modifies the optical properties of the material through a transient dielectric response, which in turn affects the absorption and reflection of the laser field. The absorbed energy is finally transferred to the thermal module to evaluate electron heating and the subsequent material response.

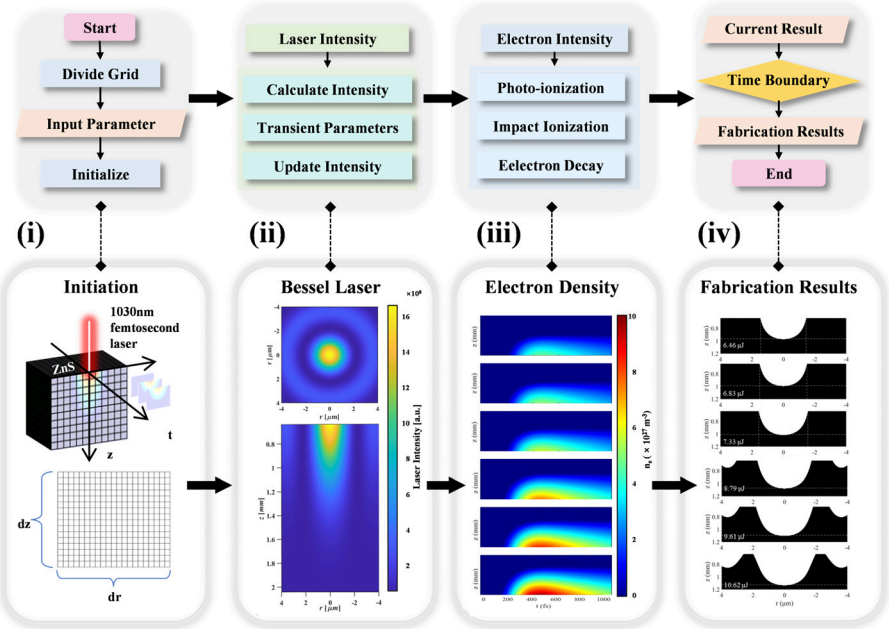

Figure 2. Numerical framework for simulating Bessel-beam interaction with ZnS, integrating laser-field propagation, plasma generation, and energy coupling. (**i**) Axisymmetric r−z coordinate system and mesh design, including high−resolution and coarse−resolution regions. (**ii**) Simulated Bessel beam intensity distribution used as the optical input for plasma calculations. (**iii**) Spatiotemporal evolution of free−electron density driven by multiphoton and avalanche ionization. (**iv**) Ablation region predicted using the critical free-electron density criterion.

The optical input used in the simulation corresponds to the intensity distribution of a Bessel beam generated by an axicon and further focused by a 4f imaging system. The scaling factor of the 4f system is defined as $\Gamma = f_1/f_2$. In this study, a plano-convex lens with focal length f_1 = 150 mm and a 20× objective lens with an equivalent focal length of f_2 = 9 mm is employed, yielding a magnification factor of Γ = 16.67. After beam compression, the spatiotemporal intensity distribution of the Bessel beam can be expressed as [43].

$$I(z,r,t) = \frac{4P(t)k\sin\beta'}{\omega_0'}\frac{z}{Z'_{max}}J_0^2(kr\sin\beta')\exp\left(-\frac{2z^2}{z'^2_{max}}\right) \quad (1)$$

where J_0 is the zeroth-order Bessel function, P(t) denotes the temporal pulse power, k is the wave number, and β' represents the propagation angle after the 4f system. The first zero of the Bessel beams after focusing occurs at approximately 1.20 μm, which is defined as the effective beam radius. This intensity distribution serves as the optical source term for the plasma simulation.

The computational domain adopts an axisymmetric r–z coordinate system, as shown in Figure 2i. The radial direction extends from 0 to 150 μm, while the axial direction spans from 0 to 568.08 μm, corresponding to the effective propagation range of the Bessel beam. To balance numerical accuracy and computational efficiency, the domain is divided into two regions with different mesh resolutions. Region 1 (r = 0–2.0 μm, z = 0–7.57 μm), where the laser energy is highly concentrated, employs a fine grid spacing of 2.0 nm in the radial direction and 7.57 nm in the axial direction. Region 2 uses coarser spacings of 0.5 μm and 1.89 μm, respectively. The outer radial boundary and the upper and lower surfaces are treated as adiabatic boundaries. During the simulation, the spatiotemporal evolution of free-electron density is calculated by considering both multiphoton ionization and avalanche ionization processes. The electron density evolution follows [44].

$$\frac{\partial n_e}{\partial t} = (W_{PI} + Q_{av})\frac{n_a}{n_0}, \tag{2}$$

where W_{PI} and Q_{av} represent the photoionization rate and avalanche ionization rate, respectively, n_0 is the atomic density of the dielectric, and n_a is the transient neutral atom density. In the present model, the photoionization rate is approximated by the multiphoton ionization (MPI) formulation [45].

$$W_{PI} = \beta_{PI} I^{k_{MPI}}, \tag{3}$$

where βMPI denotes the multiphoton ionization coefficient, k_{MPI} represents the number of photons involved in the ionization process, and I is the local laser intensity. The parameters β_{MPI} and k_{MPI} used in the simulation are listed in Table 1. This formulation is consistent with the Keldysh theory in the multiphoton regime under the present laser conditions. The generated free electrons strongly modify the optical properties of the material through the transient dielectric function. In this work, a modified Drude [46] model is adopted to describe the complex dielectric response [47].

$$\varepsilon(n_e) = \varepsilon_r + i\varepsilon_i = 1 + \left(\frac{n_e e^2}{m_e \varepsilon_0}\right)\left(\frac{-\tau_e^2 + i\tau_e/\omega}{1 + \omega^2\tau_e^2}\right), \tag{4}$$

where τ_e denotes the electron relaxation time. The effective collision frequency $\nu_e = {\tau_e}^{-1}$ includes contributions from electron–phonon, electron–electron, electron–ion, and electron–neutral collisions. These collision processes are described by semi-empirical relations, enabling the model to account for plasma heating and carrier scattering effects under ultrafast excitation. From the complex dielectric function, the refractive index f_1 and extinction coefficient f_2 can be derived, allowing the laser absorption coefficient α_e and optical reflectivity R to be calculated using Fresnel relations [48,49].

$$\alpha_e = \frac{2\omega f_2}{c}, \tag{5}$$

$$R = \frac{(f_1 - 1)^2 + f_2^2}{(f_1 + 1)^2 + f_2^2}, \tag{6}$$

These parameters determine the instantaneous energy deposition inside the material. The absorbed energy is subsequently coupled into a thermal module. Electron heating induced by laser absorption increases the electron temperature, while energy is gradually transferred to the lattice through electron–phonon coupling. The heat transfer process is solved using a two-dimensional heat conduction equation under explicit finite-difference formulation, where numerical stability is ensured through the Fourier number criterion.

Material ablation is predicted using the critical free-electron density criterion. Once the electron density approaches the critical value [50].

$$n_{cr} = \frac{4\pi^2 c^2 m_e \varepsilon_0}{\lambda^2 e^2}, \quad (7)$$

the dielectric exhibits a transition from insulating to metallic behavior, leading to strong energy absorption and subsequent material removal. It should be noted that this critical density criterion represents a necessary but not sufficient condition for material removal: reaching n_{cr} indicates a dielectric-to-metallic transition with enhanced absorption, while actual ablation additionally involves electron-phonon energy transfer and lattice heating on picosecond timescales. The quantitative discrepancy between the optically modified volume and the physically removed volume constitutes the primary correction target for the data-driven model described in Section 2.3. In the subsequent deep learning model, this threshold is used only as a normalization reference rather than a physically enforced constraint. The material and plasma parameters used in the simulation are summarized in Table 1. These parameters are taken from reported experimental and theoretical studies on ZnS and ultrafast laser–dielectric interactions. The resulting ablation morphology is obtained by tracking the spatial region where the electron density exceeds the critical threshold.

Table 1. Material and plasma parameters of ZnS used in the numerical simulation.

Parameter	Description	Value
ρ	Density of ZnS	4.09×10^3 kg/m^3
E_g	Bandgap energy	3.7 eV
n_0	Linear refractive index	2.35
ε	Dielectric constant	3.7
β_{MPI}	Multiphoton ionization coefficient	3.54×10^{-67}
k_{MPI}	Number of photons in MPI process	3
α_{imp}	Impact ionization coefficient	4×10^{-4} m^2/J
τ_e	Electron relaxation time	800 fs
n_{cr}	Critical electron density	1.05×10^{27} m^{-3}

2.3. Plasma Data-Driven Depth Correction Model

Although the plasma-based model provides reliable predictions of the in-plane feature size, noticeable discrepancies remain between the simulated and experimental ablation depths. These deviations originate from the complexity of vertical energy transport, material inhomogeneity, and simplifications in the plasma approximation. To improve the prediction accuracy, a physics data-based modeling framework was established, as illustrated in Figure 3a. The approach combines physically meaningful descriptors extracted from the plasma simulation with a data-driven regression model.

Specifically, spatial distributions of peak electron density generated by the plasma simulation were used as physically meaningful input features for the learning model. After standardized preprocessing, these features were fed into a well-established residual deep neural network designed for depth prediction. The architecture of the regression model is shown in Figure 3b. The network adopts three stacked residual blocks [51] with ReLU activation functions, leveraging the proven capability of residual learning in identity mapping and gradient flow preservation. Rather than introducing architectural novelty, the key idea is to formulate the depth prediction as a bias correction task: the model learns systematic deviations between physics-based predictions and experimental observations. By preserving information flow across network layers, the residual architecture

improves training stability and enhances generalization performance while maintaining physical interpretability.

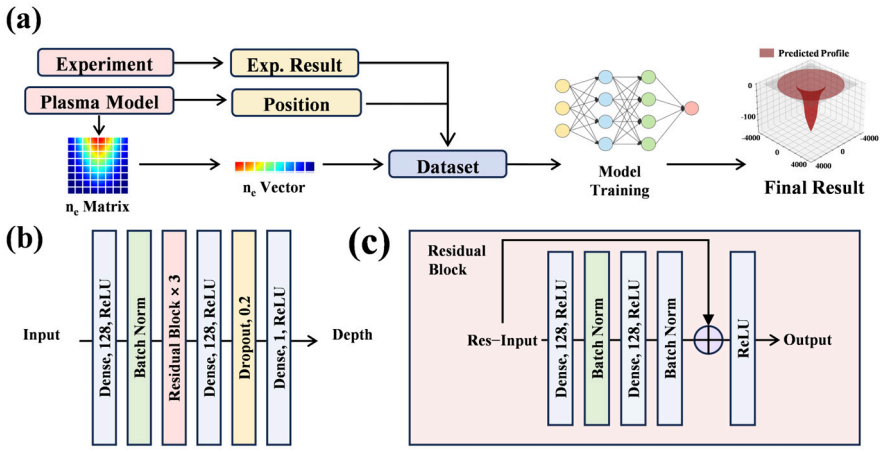

Figure 3. Deep learning correction framework based on plasma model. (**a**) Physics-data hybrid workflow integrating plasma-model descriptors with deep learning. (**b**) Residual regression network with three stacked residual blocks for depth correction. (**c**) Residual module architecture.

To ensure reproducibility and provide a complete description of the learning procedure, the dataset construction, training configuration, validation strategy, and reproducibility settings are detailed. The training dataset comprises 6408 independent depth samples extracted from 8 laser-machined craters, each corresponding to a distinct single-pulse energy level (3.93, 4.45, 6.43, 7.73, 9.03, 11.34, 12.24, and 12.80 μJ). Each sample consists of a depth measurement at a specific radial coordinate and a 43-dimensional input feature vector, including pulse energy, radial coordinate (nm), and electron density values over 41 simulation time steps. The electron density values were normalized by the critical electron density (Table 1 Critical electron density, $n_{cr} = 1.05 \times 10^{27}$ m^{-3}) and shifted by subtracting unity to obtain relative density variations. All input features were standardized to zero mean and unit variance using StandardScaler, with scaling parameters fitted exclusively on the training partition to avoid data leakage.

The model was trained using the Adam optimizer with a learning rate of 0.001 and mean squared error loss. The batch size was set to 32, and training was conducted for up to 200 epochs. To mitigate overfitting, four regularization strategies were adopted, including L2 weight regularization ($\lambda = 1 \times 10^{-4}$), dropout at a rate of 0.2, batch normalization after dense layers, and early stopping with a patience of 20 epochs based on validation loss, restoring the best-performing weights. The model contains 114,817 trainable parameters. To avoid spatial data leakage between neighboring samples from the same crater, crater-level grouped cross-validation was employed. Specifically, GroupKFold with $K = 3$ was adopted using crater identity as the grouping variable. Additionally, Leave-One-Group-Out (LOGO) cross-validation was conducted, in which each energy level was sequentially used as the test set while the remaining samples were used for training.

To assess prediction reliability, we employed Monte Carlo Dropout (MC Dropout) [52] for uncertainty quantification. During inference, the Dropout layers (rate = 0.2) within each residual block were kept active, and 100 stochastic forward passes were performed for each test sample. The mean of the 100 predictions serves as the point estimate, while the standard deviation quantifies the epistemic uncertainty—representing the model's lack of knowledge about the true mapping function.

All experiments were made fully reproducible by fixing random seeds (seed = 42) for Python random 3.8.10, NumPy 1.24.3, and TensorFlow 2.13.0. The specific versions adopted

in this work are Python 3.8.10, NumPy 1.24.3 and TensorFlow 2.13.0, ensuring consistent initialization, data shuffling, and training behavior across runs.

3. Results

3.1. Plasma Simulation and Experimental Comparison

The microstructures produced by single-point Bessel-beam irradiation were characterized using confocal microscopy. Representative modification regions are shown in Figure 4a, revealing well-defined circular features formed within the ZnS substrate. The dependence of the processed feature size on the incident laser energy was systematically investigated. Figure 4b presents the measured diameters of the modification zones as a function of pulse energy. The diameter increases monotonically with increasing energy, reflecting the larger region exceeding the modification threshold. To further analyze the scaling behavior, the diameter–energy relationship is plotted on a logarithmic scale in Figure 4c. The results reveal an approximately exponential growth trend, suggesting a strong nonlinear dependence of modification size on laser energy.

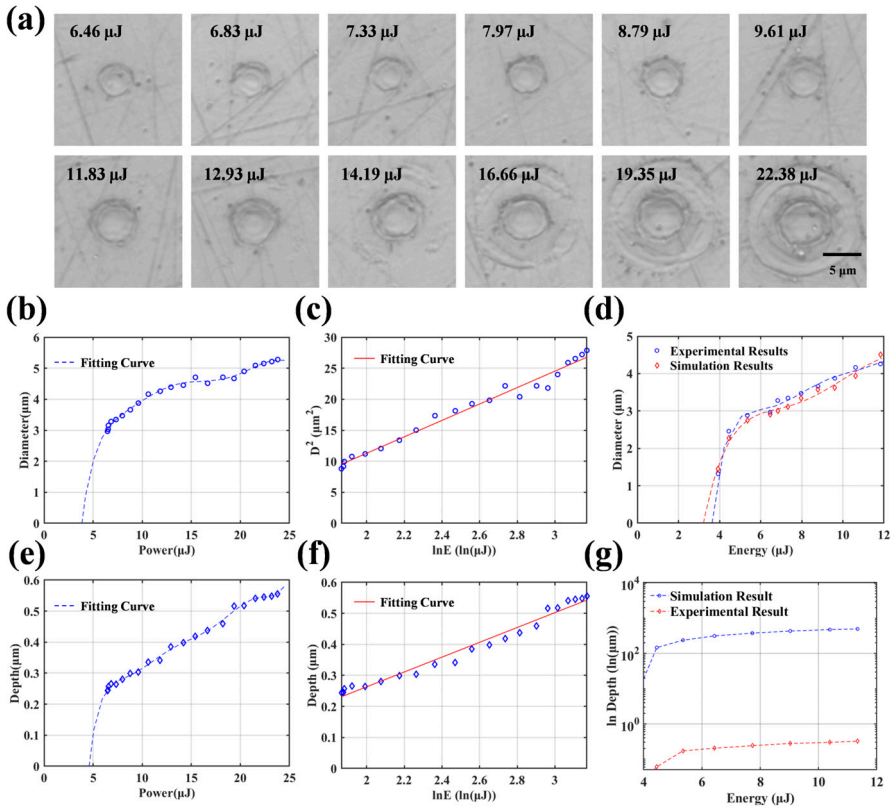

Figure 4. Experimental characterization of modification size versus pulse energy. (**a**) Confocal images of single-point modification zones. (**b**) Diameter–energy relation and (**c**) its logarithmic scaling. (**d**) Ablation diameter comparison between simulation and experiment. (**e**) Depth–energy dependence and (**f**) corresponding logarithmic plot. (**g**) Ablation depth comparison between simulation and experiment.

Similarly, the evolution of the modification depth with increasing pulse energy is shown in Figure 4e. The ablation depth increases steadily as the deposited energy rises. The corresponding logarithmic representation in Figure 4f indicates a predictable scaling behavior, confirming that the internal feature dimensions in ZnS can be effectively controlled by tuning the laser energy.

The plasma-based numerical model was used to simulate the ablation process under the same experimental conditions. Quantitative comparisons of the feature diameter and

depth are presented in Figures 4d and 4g, respectively. The simulated diameters exhibit strong agreement with experimental measurements, with an average relative error of approximately 4.8%. In contrast, the depth prediction shows larger deviations, indicating potential limitations in modeling vertical energy transport and material response.

3.2. Ultrafast Carrier Dynamics in ZnS

The ultrafast evolution of laser-induced excitation in ZnS was investigated using pump–probe measurements. Time-resolved relative-reflectivity images recorded at different excitation energies are shown in Figure 5a. A clear difference between low- and high-fluence excitation conditions can be observed. At higher energies, the region exhibiting strong reflectivity change becomes significantly broader due to the Gaussian spatial profile of the laser beam. At early delay times, the radial profiles of the relative reflectivity can be well fitted by Gaussian functions, indicating that the initial excitation distribution closely follows the laser intensity profile.

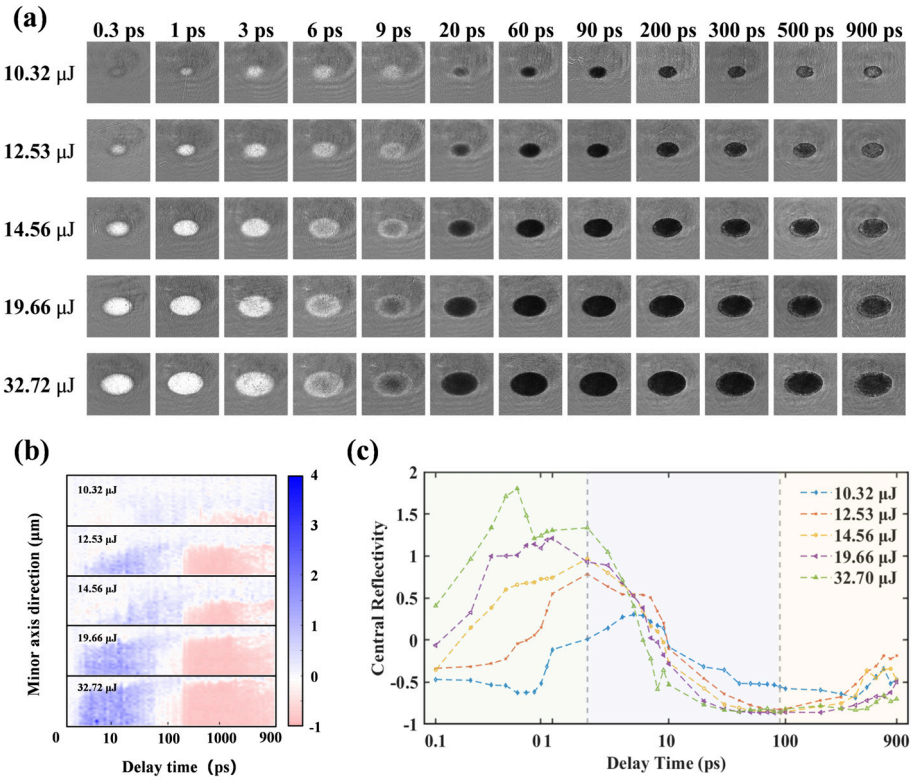

Figure 5. Ultrafast pump-probe characterization of femtosecond excitation in ZnS. (**a**) Time resolved relative-reflectivity images under varying fluences, showing broader excitation at higher energy. (**b**) Temporal reflectivity dynamics revealing rapid rise at high fluence and non-monotonic response at low fluence. (**c**) Simulated three-stage electron-density evolution governed by photoionization, avalanche ionization, and saturation.

As the system evolves in time, the reflectivity profiles gradually deviate from the Gaussian shape and tend toward a quasi–flat-top distribution, reflecting the saturation of carrier density in the central region. The temporal reflectivity evolution is shown in Figure 5b. Under high-fluence excitation, the reflectivity increases rapidly and reaches its maximum within an ultrashort timescale. In contrast, at low fluence, the reflectivity initially decreases and subsequently increases, exhibiting a non-monotonic response. These observations are consistent with the simulated electron-density evolution shown in Figure 5c. The excitation process can be divided into three stages: an initial photoionization stage, a rapid avalanche

ionization stage, and a final saturation stage where the free-electron density approaches its maximum value.

3.3. Prediction Results of the Corrected Model

The predictive capability of the deep learning model was evaluated using both single-sample analysis and large-scale dataset statistics. Figure 6a,b compares the experimentally measured three-dimensional crater morphology with the model prediction at a pulse energy of 5.35 μJ. The predicted crater shape accurately reproduces the overall contour and maximum-depth location observed in the experimental data.

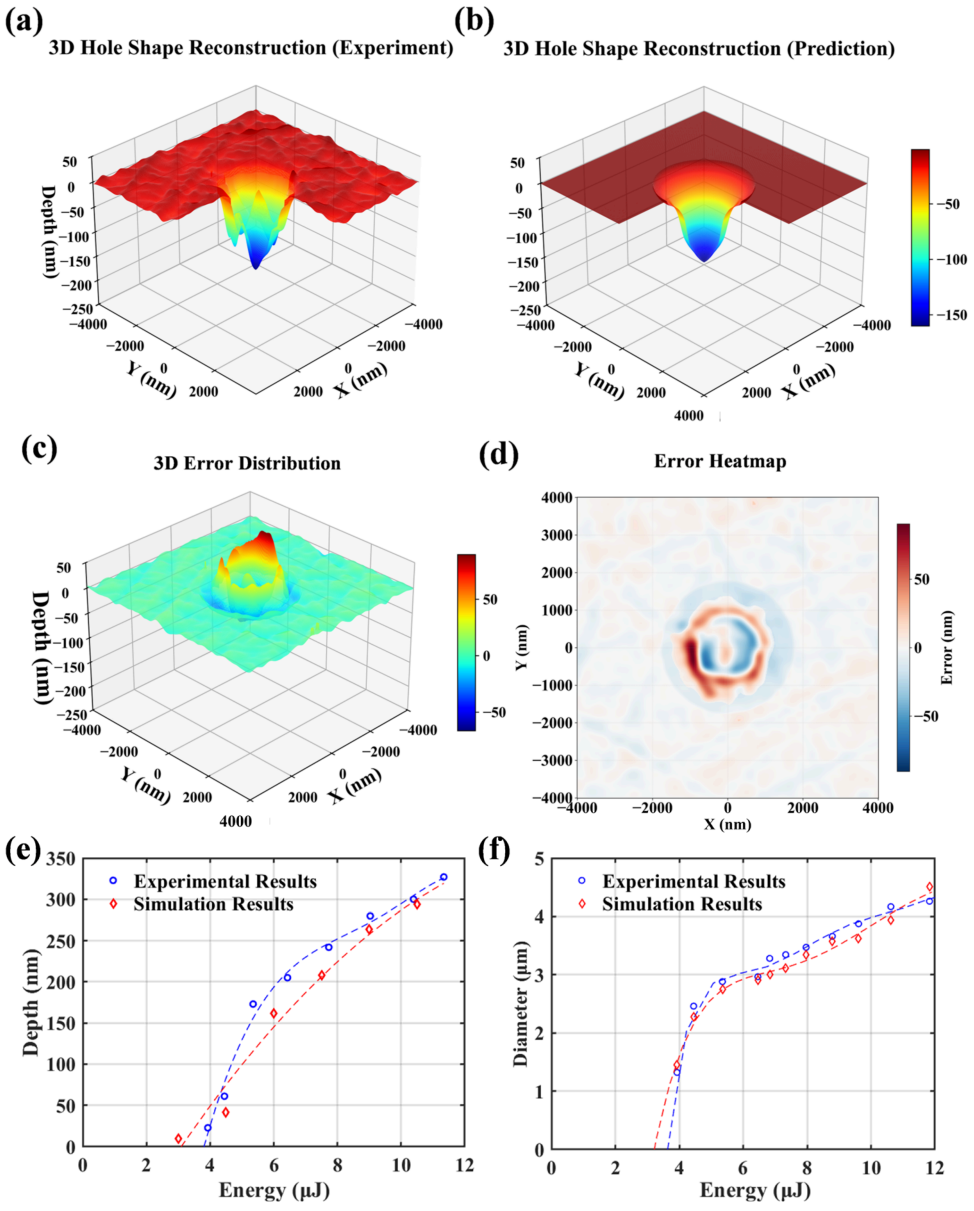

Figure 6. Prediction performance of the proposed deep-learning model. (**a**) Measured and (**b**) predicted 3D crater morphology at 5.35 μJ. (**c**) Point-wise error map and (**d**) error-distribution heatmap, showing most errors within ±50 nm. (**e**) Predicted vs. measured crater depth across pulse energies. (**f**) Comparison of lateral diameters showing no systematic deviation.

The point-wise error map obtained by subtracting the predicted and measured surfaces is shown in Figure 6c. Most errors fall within ±50 nm and exhibit a relatively uniform spatial distribution. The error-distribution heatmap in Figure 6d further confirms the

absence of significant local deviations. A magnified view of the crater bottom demonstrates that the model maintains stable prediction accuracy in the depth-dominated region without systematic error accumulation. For 3D morphology reconstruction, the 1D radial depth prediction is rotated around the beam axis to reconstruct the full crater surface (~640,000 pixels for the 5.35 μJ case). Pixel-level evaluation reflects smooth geometric consistency, but these pixels are not independent samples since they are derived from ~800 radial predictions via rotational symmetry. Therefore, statistical validity should be assessed at the independent-crater level rather than pixel level. At this level, the model shows strong performance under random split, while more rigorous crater-grouped and LOGO evaluations reveal a substantial drop in accuracy, indicating that spatially aware validation provides a more realistic estimate of generalization to unseen craters. Across different pulse energies (Figure 6e), the predicted depths closely follow the experimental trend, while the lateral diameters (Figure 6f) also match the measurements without systematic deviation.

3.4. Model Comparison and Cross-Validation

To validate the effectiveness of the residual network architecture, we performed a model comparison under identical evaluation conditions. Four models were evaluated using the same 8-fold cross-validation: (1) the proposed ResNet with residual connections; (2) a Plain MLP with identical configuration but without skip connections (ablation study); (3) Random Forest (100 estimators, max depth = 20); and (4) Gradient Boosting (100 estimators, max depth = 6, learning rate = 0.1). All models used the same 43-dimensional input features and were evaluated on identical test partitions to ensure strict comparability.

The proposed ResNet achieves the best average performance across all metrics (MAE = 14.87 nm, RMSE = 20.45 nm, R^2 = 0.748), as shown in the Table 2, confirming the effectiveness of residual connections for physics-model correction tasks. Removing skip connections increases MAE from 14.87 to 15.36 nm (3.3% degradation) and reduces R^2 from 0.748 to 0.499 (33.3% degradation). The larger reduction in R^2 suggests skip connections are critical for stable generalization across different energy conditions. The Plain MLP also shows the largest R^2 variance (0.889), indicating unstable performance across folds. Both tree-based models yield higher MAE (17.49 and 16.57 nm) and lower mean R^2 than the ResNet. Notably, Gradient Boosting achieves the best single-fold performance at 3.93 μJ (MAE = 4.00 nm), but its overall generalization is weaker. The per-energy analysis shows that the ResNet achieves the lowest MAE in 4 of 8 conditions, while no baseline consistently dominates. To further evaluate data partitioning effects, two crater-grouped cross-validation schemes were used in addition to the random split baseline.

Table 2. Performance comparison of different models under cross-validation.

Model	MAE (nm)	RMSE (nm)	R^2
ResNet (proposed)	14.87 ± 8.45	20.45 ± 10.89	0.748 ± 0.336
Plain MLP (no skip)	15.36 ± 6.59	22.14 ± 8.87	0.499 ± 0.889
Random Forest	17.49 ± 8.79	23.87 ± 12.24	0.652 ± 0.456
Gradient Boosting	16.57 ± 8.79	22.90 ± 11.55	0.660 ± 0.511

The LOGO results show a clear energy-dependent generalization pattern in the Tables 3 and 4. The model achieves strong performance ($R^2 > 0.95$) for energies in the 9.03–12.24 μJ range, where training data provide neighboring conditions that bracket the test samples. In contrast, performance degrades at the range extremes, reaching R^2 = 0.483 at 4.45 μJ and $R^2 = -0.028$ at 3.93 μJ, which lies near the damage threshold. The negative R^2 at 3.93 μJ indicates worse-than-mean prediction performance. This suggests that

physical processes near the damage threshold differ qualitatively, including a transition from multi-photon ionization to tunneling ionization and stochastic nucleation effects, which cannot be reliably interpolated from higher-energy data. These results imply that the model should not be applied below the lowest training energy without additional calibration. Comparing random split (R^2 = 0.971) with grouped evaluation (GroupKFold R^2 = 0.839, LOGO R^2 = 0.743) shows that spatial leakage inflates reported performance. The reduction of 13–23 percentage points reflects the true generalization gap previously hidden by random splitting.

Table 3. GroupKFold (K = 3) cross-validation results.

Fold	MAE (nm)	RMSE (nm)	R^2
1	31.19	55.43	0.726
2	22.73	37.47	0.855
3	16.29	25.27	0.935

Table 4. Leave-One-Group-Out (LOGO) cross-validation results by energy level.

Energy (μJ)	MAE (nm)	RMSE (nm)	R^2
3.93	55.43	6.35	0.028
4.45	37.47	9.24	0.483
6.43	25.27	29.57	0.776
7.73	21.84	30.74	0.859
9.03	16.55	21.83	0.953
11.34	13.59	18.52	0.977
12.24	8.75	11.17	0.992
12.80	28.12	35.08	0.931

MC Dropout maintains strong predictive performance (MAE = 11.39 nm, RMSE = 17.12 nm, R^2 = 0.972) as shown in the Table 5, while providing stochastic uncertainty estimates that correlate with prediction errors. The uncertainty distribution is highly skewed, with a substantially lower median (1.62 nm) than mean (6.71 nm), indicating that most samples are predicted with high confidence, while a small subset exhibits elevated epistemic uncertainty. This behavior is consistent with physically challenging regions such as boundary or transition zones. Overall, the results suggest that MC Dropout provides a useful, albeit not fully calibrated, measure of predictive reliability.

Table 5. MC Dropout evaluation.

Metric	Value
MC mean MAE (nm)	11.39
MC mean RMSE (nm)	17.12
MC mean R^2	0.972
Mean uncertainty σ (nm)	6.71
Median uncertainty σ (nm)	1.62

4. Discussion

The combined experimental, numerical, and data-driven results provide a comprehensive understanding of femtosecond Bessel-beam processing of ZnS. The plasma-based simulation successfully captures the primary physical mechanisms governing electron generation and energy deposition, enabling accurate prediction of the ablation diameter. However, the simulation exhibits noticeable discrepancies in predicting the ablation depth. These deviations likely arise from simplified assumptions in the thermal transport model,

uncertainties in material parameters, and the complex interaction between plasma expansion and lattice dynamics. Specifically, the lateral crater dimensions are primarily governed by the well-characterized intensity distribution of the central lobe of the Bessel beam, whereas material removal along the depth direction involves successive layer-by-layer energy deposition with nonlinearly evolving plasma absorption coefficients. This process forms a coupled feedback mechanism that is not iteratively resolved by the current single-pass simulation. Furthermore, the simulation is restricted to the femtosecond temporal regime and does not capture post-pulse material removal dynamics, including shock wave propagation, phase explosion, and spallation, which predominantly influence the depth direction. The rapid accumulation of free electron density also induces transient changes in the refractive index and plasma shielding effects, thereby reducing energy deposition in deeper regions. This self-limiting mechanism exhibits an inherent dependence on depth. These systematic discrepancies between the physical model and experimental observations define the target of the residual learning strategy. The LOGO cross-validation results in Table 4 provide quantitative evidence. The model achieves $R^2 > 0.95$ at higher energies in the range of 9.03~12.24 μJ, but its performance degrades to $R^2 = -0.028$ at 3.93 μJ near the damage threshold, where the nonlinear mechanisms become dominant.

By integrating physically meaningful descriptors derived from the plasma simulation with a deep learning regression model, the hybrid framework effectively compensates for these limitations. The data-driven correction captures nonlinear relationships between plasma density distribution and final ablation depth that are difficult to model analytically. The proposed approach demonstrates that combining physics-based modeling with machine learning can significantly enhance predictive capability while retaining interpretability. Such hybrid strategies may be extended to other transparent materials and complex beam configurations in femtosecond laser processing. It should be noted that ZnS has a zinc blende (cubic, F-43m) structure and is optically isotropic under linear conditions. In this work, the CVD-grown ZnS is polycrystalline, so orientation-dependent nonlinear effects are statistically averaged over randomly oriented grains, making macroscopic anisotropy negligible. The observed rotational symmetry of crater morphologies further supports this assumption. Moreover, polycrystalline ZnS is the dominant industrial form for infrared applications due to its lower cost, making the isotropic model practically relevant.

5. Conclusions

This study systematically investigates femtosecond Bessel-beam processing of zinc sulfide and proposes a hybrid modeling framework combining plasma-based simulations with data-driven learning. A plasma dynamics model incorporating multiphoton ionization, collisional ionization, and Drude free-electron dynamics was developed to describe the interaction between femtosecond laser pulses and ZnS. The model successfully predicts the ablation diameter and reproduces key trends observed in the experiments. Pump–probe measurements further reveal the ultrafast carrier dynamics during laser excitation, confirming the simulated three-stage evolution of electron density.

To address the limitations of physics-based depth prediction, a lightweight deep learning regression model was introduced using plasma-derived descriptors as input features. While the pixel-level reconstruction accuracy demonstrates the model's utility for 3D morphology prediction, the crater-grouped cross-validation provides a more conservative and representative assessment of generalization performance. The proposed physics–data integrated strategy provides an effective tool for predictive modeling and process optimization in femtosecond laser micro- and nanofabrication and can be readily extended to other materials and advanced beam engineering schemes.

https://doi.org/10.3390/photonics13040394

Author Contributions: Conceptualization, Y.D. and J.S.; methodology, J.S.; software, Y.D. and X.D.; validation, Y.D., M.Y. and X.D.; formal analysis, Y.D. and Y.Y.; investigation, Y.D.; resources, J.S.; data curation, Y.D. and X.L.; writing—original draft preparation, Y.D.; writing—review and editing, Y.D. and J.S.; visualization, Y.D.; supervision, J.S.; project administration, J.S.; funding acquisition, J.S. All authors have read and agreed to the published version of the manuscript.

Funding: This work was supported by the National Key Research and Development Program of China (Grant No.2023YFB4605501), National Natural Science Foundation of China (Grant No. 62175253) and CAS Project for Young Scientists in Basic Research (Grant No. YSBR-056).

Institutional Review Board Statement: Not applicable.

Informed Consent Statement: Not applicable.

Data Availability Statement: Data underlying the results presented in this paper are not publicly available at this time but may be obtained from the authors upon reasonable request.

Conflicts of Interest: The authors declare no conflicts of interest.

Abbreviations

ZnS	Zinc sulfide
MAE	Mean absolute error
RMSE	Root mean square error
ReLU	Rectified linear unit
MPI	Multiphoton ionization

References

1. An, Y.; Lei, M.; Chang, C.; Xiong, L.; Chen, X.; Zhang, G.; Gao, W. Investigations on the quality improvement of laser processing for LN. *Opt. Laser Technol.* **2023**, *161*, 109231. [CrossRef]
2. Ardaneh, K.; Hassan, M.; Morel, B.; Meyer, R.; Giust, R.; Couairon, A.; Bonnaud, G.; Courvoisier, F. Femtosecond laser-induced sub-wavelength plasma inside dielectrics. II. Second-harmonic generation. *Phys. Plasmas* **2022**, *29*, 072716. [CrossRef]
3. Ardaneh, K.; Meyer, R.; Hassan, M.; Giust, R.; Morel, B.; Couairon, A.; Bonnaud, G.; Courvoisier, F. Femtosecond laser-induced sub-wavelength plasma inside dielectrics: I. Field enhancement. *Phys. Plasmas* **2022**, *29*, 072715. [CrossRef]
4. Bleyan, Y.; Sargsian, T.; Kostanyan, A.; Hayrapetyan, D.; Mantashyan, P.A. Impact of intense laser Bessel beam on excitonic complexes in ellipsoidal quantum dot. *J. Lumin.* **2023**, *263*, 120101. [CrossRef]
5. Cheng, J.; Liao, J.; He, Z.; Zhang, L.; Liu, B.; Chen, L.; Yang, Q.; Lou, D.; Tao, Q.; Li, Q. Continuous GHz femtosecond laser interacting with aluminum film: Simulation and experiment. *Opt. Laser Technol.* **2024**, *175*, 110792. [CrossRef]
6. Enrico, A.; Buchmann, S.; De Ferrari, F.; Lin, Y.; Wang, Y.; Yue, W.; Mårtensson, G.; Stemme, G.; Hamedi, M.M.; Niklaus, F. Cleanroom-Free Direct Laser Micropatterning of Polymers for Organic Electrochemical Transistors in Logic Circuits and Glucose Biosensors. *Adv. Sci.* **2024**, *11*, 2307042. [CrossRef]
7. Guo, B.; Song, Z. High-Efficiency Targeted Gene Transfection of Cells Using Temporal and Spatial Shaping Femtosecond Laser Irradiation. *J. Biophoton.* **2025**, *18*, e202400409. [CrossRef] [PubMed]
8. Hattori, J.; Ito, Y.; Sugita, N. Crackless femtosecond laser percussion drilling of SiC by suppressing shock wave magnitude. *CIRP Ann.* **2023**, *72*, 185–188. [CrossRef]
9. He, Z.; Lei, L.; Lin, S.; Tian, S.; Tian, W.; Yu, Z.; Li, F. Metal material processing using femtosecond lasers: Theories, principles, and applications. *Materials* **2024**, *17*, 3386. [CrossRef]
10. Yang, J.; Zhou, S.; Yang, M.; Zhao, S.; Wang, S.; Deng, G. Antireflection microstructures on a ZnS surface fabricated by femtosecond laser direct writing assisted with wet etching. *Opt. Mater.* **2025**, *159*, 116597. [CrossRef]
11. Ding, Y.; Wang, C.; Jia, X.; Liu, L.; Gao, Z.; Jiang, X.; Wang, S.; Yan, D.; Lin, N.; Duan, J.-a. Biomimetic ZnS windows fabricated by femtosecond laser optical field modulation assisted with wet etching for high-performance infrared monitoring of EV charging. *ACS Appl. Mater. Interfaces* **2025**, *17*, 42462–42473. [CrossRef]
12. Zhang, H.; Li, Q.; Zheng, H.; Jiang, J.; Hong, W.; Zhang, L.; Liu, Y. High-quality customized micro-diffractive optical devices fabricated from ZnS ceramics using femtosecond laser direct writing and solution etching. *Ceram. Int.* **2025**, *51*, 10521–10532. [CrossRef]
13. Ianhez-Pereira, C.; Kuriakose, A.; Rodrigues, A.D.G.; Silva, A.L.C.; Jedrkiewicz, O.; Bollani, M.; de Godoy, M.P.F. Evaluation of microscale crystallinity modification induced by laser writing on Mn_3O_4 thin films. *Opt. Mater.* **2024**, *147*, 114609. [CrossRef]

14. Jing, X.; Li, S.; Zhu, R.; Ning, X.; Lin, J. Miniature bioinspired artificial compound eyes: Microfabrication technologies, photodetection and applications. *Front. Bioeng. Biotechnol.* **2024**, *12*, 1342120. [CrossRef]
15. Kai, L.; Chen, C.; Lu, Y.; Meng, Y.; Liu, Y.; Cheng, Y.; Yang, Q.; Hou, X.; Chen, F. Insight on the regulation mechanism of the nanochannels in hard and brittle materials induced by sparially shaped femtosecond laser. *Front. Chem.* **2022**, *10*, 973570. [CrossRef] [PubMed]
16. Leng, R.-Z.; Yun, B.; Chen, Z.-H.; Chai, C.; Xu, W.-W.; Yu, Y.-H.; Wang, L. High-Transmission Biomimetics Structural Surfaces Produced via Ultrafast Laser Manufacturing. *Biomimetics* **2023**, *8*, 586. [CrossRef] [PubMed]
17. Li, J.; Yan, J.; Jiang, L.; Qu, L. Chiral lithography with vortex non-diffracted laser for orbital angular momentum detection. *Laser Photonics Rev.* **2024**, *18*, 2301050. [CrossRef]
18. Li, X.; Li, M. Broadband antireflective hybrid micro/nanostructure on zinc sulfide fabricated by optimal Bessel femtosecond laser. *Nanomaterials* **2023**, *13*, 1225. [CrossRef]
19. Li, X.; Ye, B.; Jiang, L.; Li, X.; Zhao, Y.; Qu, L.; Yi, P.; Li, T.; Li, M.; Li, L. Helical Micropillar Processed by One-Step 3D Printing for Solar Thermal Conversion. *Small* **2024**, *20*, 2400569. [CrossRef]
20. Stoian, R.; Bhuyan, M.K.; Zhang, G.; Cheng, G.; Meyer, R.; Courvoisier, F. Ultrafast Bessel beams: Advanced tools for laser materials processing. *Adv. Opt. Technol.* **2018**, *7*, 165–174. [CrossRef]
21. Dynevik, P.; Severinson, N. Capability determination of in-process monitoring for laser powder bed fusion. *Micromachines* **2025**, *13*, 1366. [CrossRef]
22. Lim, D.-W.; Kim, M.; Choi, P.; Yoon, S.-J.; Lee, H.-T.; Kim, K. Hole depth prediction in a femtosecond laser drilling process using deep learning. *Micromachines* **2023**, *14*, 743. [CrossRef]
23. Liu, D.-C.; Li, P.-Y.; Zhu, T.-X.; Zheng, L.; Huang, J.-Y.; Zhou, Z.-Q.; Li, C.-F.; Guo, G.-C. On-demand storage of photonic qubits at telecom wavelengths. *Phys. Rev. Lett.* **2022**, *129*, 210501. [CrossRef]
24. Tomkus, V.; Girdauskas, V.; Abedi-Varaki, M.; Raciukaitis, G. Laser wakefield acceleration of electrons using Bessel–Gauss doughnut beams for accelerating beam guiding. *J. Plasma Phys.* **2023**, *89*, 905890209. [CrossRef]
25. Abedi-Varaki, M.; Daraei, M. Impact of wiggler magnetic field on wakefield generation and electron acceleration by Gaussian, super-Gaussian and Bessel–Gaussian laser pulses propagating in collisionless plasma. *J. Plasma Phys.* **2023**, *89*, 905890114. [CrossRef]
26. Abedi-Varaki, M.; Tomkus, V.; Girdauskas, V.; Račiukaitis, G. Influence of nitrogen concentration on laser wakefield acceleration of electrons driven by Bessel-Gauss laser beam. *Appl. Phys. A* **2025**, *131*, 192. [CrossRef]
27. Liu, Y.; Zhou, J. Editorial for the Special Issue on Recent Advances in Micro/Nano-Fabrication. *Micromachines* **2024**, *15*, 1485. [CrossRef]
28. Lutz, C.; Schwarz, S.; Marx, J.; Esen, C.; Hellmann, R. Multi-Bessel beams generated by an axicon and a spatial light modulator for drilling applications. *Photonics* **2023**, *10*, 413. [CrossRef]
29. Lv, J.; Wang, G.; Li, Y.; Li, Z.; Yu, Y.; Wang, Y.; Lv, Z. Status and applications of femtosecond laser preparation of SERS substrates containing noble metals nanoparticles. *Surf. Interfaces* **2024**, *51*, 104719. [CrossRef]
30. Ma, C.; Nikiforov, A.; Hegemann, D.; De Geyter, N.; Morent, R.; Ostrikov, K. Plasma-controlled surface wettability: Recent advances and future applications. *Int. Mater. Rev.* **2023**, *68*, 82–119. [CrossRef]
31. Qi, P.; Qian, W.; Guo, L.; Xue, J.; Zhang, N.; Wang, Y.; Zhang, Z.; Zhang, Z.; Lin, L.; Sun, C. Sensing with femtosecond laser filamentation. *Sensors* **2022**, *22*, 7076. [CrossRef]
32. Qu, Z.; Sun, S.; Wang, J.; Jiang, M.; Zhang, F.; Wang, X.; Shao, J.; Liang, G.; Wang, P. Application of ultrafast laser beam shaping in micro-optical elements. *J. Laser Appl.* **2023**, *35*, 031202. [CrossRef]
33. Singh, S.C.; Guo, C. Femtosecond laser-produced optical absorbers for solar-thermal energy harvesting. *EcoMat* **2022**, *4*, e12161. [CrossRef]
34. Wang, F.; Jiang, L.; Pan, C.; Wang, Z.; Lian, Y.; Wang, Q.; Tao, W.; Sun, J. Hologram imaging quality improvement by ionization controlling based on the self-trapped excitons with double-pulse femtosecond laser. *Nanophotonics* **2022**, *11*, 4727–4736. [CrossRef]
35. Wang, H.; Zhang, F.; Duan, J. Subwavelength quasi-periodic array for infrared antireflection. *Nanomaterials* **2022**, *12*, 3520. [CrossRef]
36. Wang, Q.; Zhang, R.; Chen, Q.; Duan, R. A review of femtosecond laser processing of silicon carbide. *Micromachines* **2024**, *15*, 639. [CrossRef] [PubMed]
37. Wang, S.; Yang, J.; Deng, G.; Zhou, S. Femtosecond laser direct writing of flexible electronic devices: A mini review. *Materials* **2024**, *17*, 557. [CrossRef]
38. Wang, Z.; Jiang, L.; Li, X.; Gao, S.; Zhou, S.; Liu, Y.; Huang, L.; Lu, J.; Yin, J. High efficiency and scalable fabrication of Fresnel zone plates using holographic femtosecond pulses. *Nanophotonics* **2022**, *11*, 3081–3091. [CrossRef]
39. Wu, J.; Huo, L.; Ni, Y.; Wu, Z.; Chen, T.; Gao, S.; Li, S. Supercontinuum induced by filamentation of Bessel-Gaussian and Laguerre-Gaussian beams in water. *Appl. Sci.* **2022**, *12*, 6005. [CrossRef]

40. Yi, C.; Qu, S.; Wang, Y.; Qi, H.; Zhang, Y.; Cheng, G.J. Optical force brush enabled free-space painting of 4D functional structures. *Sci. Adv.* **2023**, *9*, eadg0300. [CrossRef] [PubMed]
41. Zhang, F.; Wang, H.; Yin, K.; Duan, J. Antireflective array on zinc sulfide fabricated by femtosecond laser. *Opt. Laser Technol.* **2022**, *155*, 108438. [CrossRef]
42. Zhang, N.; Wang, M.; Ban, M.; Guo, L.; Liu, W. Femtosecond laser drilling 100 μm diameter micro holes with aspect ratios > 20 in a Nickel based superalloy. *J. Mater. Res. Technol.* **2024**, *28*, 1415–1422. [CrossRef]
43. Brzobohatý, O.; Čižmár, T.; Zemánek, P. High quality quasi-Bessel beam generated by round-tip axicon. *Opt. Express* **2008**, *16*, 12688–12700. [CrossRef] [PubMed]
44. Pan, P.; Ji, P.; Lin, G. Spatiotemporal probe into the femtosecond laser processing of fused silica. *Appl. Phys. A* **2022**, *128*, 854. [CrossRef]
45. Keldysh, L. Ionization in the field of a strong electromagnetic wave. In *Selected Papers of Leonid V Keldysh*; World Scientific: Singapore, 2024; pp. 56–63. [CrossRef]
46. Bulgakova, N.M.; Stoian, R.; Rosenfeld, A.; Hertel, I.; Marine, W.; Campbell, E. A general continuum approach to describe fast electronic transport in pulsed laser irradiated materials: The problem of Coulomb explosion. *Appl. Phys. A* **2005**, *81*, 345–356. [CrossRef]
47. Jiang, L.; Wang, A.-D.; Li, B.; Cui, T.-H.; Lu, Y.-F. Electrons dynamics control by shaping femtosecond laser pulses in micro/nanofabrication: Modeling, method, measurement and application. *Light: Sci. Appl.* **2018**, *7*, 17134. [CrossRef]
48. Stuart, B.C.; Feit, M.D.; Herman, S.; Rubenchik, A.; Shore, B.; Perry, M. Nanosecond-to-femtosecond laser-induced breakdown in dielectrics. *Phys. Rev. B* **1996**, *53*, 1749. [CrossRef]
49. Rethfeld, B. Unified model for the free-electron avalanche in laser-irradiated dielectrics. *Phys. Rev. Lett.* **2004**, *92*, 187401. [CrossRef]
50. Bulgakova, N.; Stoian, R.; Rosenfeld, A.; Hertel, I.; Campbell, E. Electronic transport and consequences for material removal in ultrafast pulsed laser ablation of materials. *Phys. Rev. B* **2004**, *69*, 054102. [CrossRef]
51. He, K.; Zhang, X.; Ren, S.; Sun, J. Deep residual learning for image recognition. In Proceedings of the IEEE Conference on Computer Vision and Pattern Recognition, Las Vegas, NV, USA, 27–30 June 2016; pp. 770–778. [CrossRef]
52. Gal, Y.; Ghahramani, Z. Dropout as a bayesian approximation: Representing model uncertainty in deep learning. In Proceedings of the International Conference on Machine Learning, New York, NY, USA, 19–24 June 2016; pp. 1050–1059.

Disclaimer/Publisher's Note: The statements, opinions and data contained in all publications are solely those of the individual author(s) and contributor(s) and not of MDPI and/or the editor(s). MDPI and/or the editor(s) disclaim responsibility for any injury to people or property resulting from any ideas, methods, instructions or products referred to in the content.